Chinese Chemical Letters 34 (2023) 107348

Contents lists available at ScienceDirect

Chinese Chemical Letters

journal homepage: www.elsevier.com/locate/cclet

Polyoxometalate derived p-n heterojunction for optimized reaction interface and improved HER

Xiaoli Cui [a], Yunmeng Sun [a], Xinxin Xu [a,b,*]

[a] Department of Chemistry, College of Science, Northeastern University, Shenyang 110819, China
[b] Institute for Frontier Technologies of Low-Carbon Steelmaking, Northeastern University, Shenyang 110819, China

ARTICLE INFO

Article history:
Received 18 February 2022
Revised 14 March 2022
Accepted 15 March 2022
Available online 18 March 2022

Keywords:
Polyoxometalate
p-n Heterojunction
Electrocatalysis
HER
Zn-H^+ battery

ABSTRACT

MoS_2 is a typical electrocatalyst for hydrogen evolution reaction (HER), but the HER activity is spoilt by intensive adsorption towards H^*, which requires further improvement. For n-type MoS_2, the construction of p-n heterojunction with p-type MoO_3 can reverse this situation, because inner electronic field in p-n heterojunction can facilitate H^* desorption. Based on this hypothesis, p-n heterojunction is built between MoS_2 and MoO_3 with polyoxometalate compound as precursor. The obtained MoO_3/MoS_2 exhibits excellent HER activity, which only requires 68 mV to obtain 10 mA/cm^2. With MoO_3/MoS_2 as cathode material and Zn slice as anode, Zn-H^+ battery is assembled. Its open circuit voltage achieves 1.11 V with short circuit current 151.4 mA/cm^2. The peak power density of this Zn-H^+ battery reaches 47.6 mW/cm^2. When discharge at 10 mA/cm^2, the specific capacity and energy density reach 728 mAh/g and 759 Wh/kg. In this process, H_2 production rate of Zn-H^+ battery achieves 364 μmol/h with Faradic efficiency 97.8%. It realizes H_2 production and electricity generation simultaneously.

Recently, worsening global environment and exhausted non-renewable energy have forced human to seek clean and green renewable source as substitute for traditional fossil fuels [1]. As one of the most perspective members in new breed of energy carrier, H_2 can offer human being with adequate, sustainable and pollution-free energy supply, which has been considered as an important participant for the construction of energy infrastructure in the future [2,3]. For H_2, to realize large scale application, production method is the most important segment [4]. Electrocatalytic water splitting is a clean and perspective way for H_2 production [5–7]. Compared with other H_2 production technology, it is a fascinating and promising method, which exhibits low cost, simple operation and zero discharge [8–10]. With promotion of electrocatalyst, HER occurs and generates H_2 efficiently [11–13]. Pt based materials are well-known HER electrocatalysts [14]. But their massive popularization in H_2 production is severely limited by expensive price, low reserve and poor stability [15–18]. Currently, design and exploration of stable, cut-price HER electrocatalyst with high efficiency becomes the first issue to achieve scalable H_2 production [19–21].

As a prolific and high performance electrocatalyst, MoS_2 exhibits graphene shaped two-dimensional layer structure, which is regarded as a prospective choice for H_2 production [22–26]. Hexagonal symmetry MoS_2 (2H-MoS_2) and tetragonal phase MoS_2 (1T-MoS_2) are the most common phase in MoS_2 [27]. By and large, 2H-MoS_2 possesses more superior HER activity over 1T-MoS_2 [28]. But 2H-MoS_2 also has a fatal weakness in HER, improper H^* adsorption free energy (ΔG_{H^*}) [29]. For an electrocatalyst, HER activity is largely determined by its interaction with adsorbed H (H^*) [30]. In 2H-MoS_2, d orbital shows intensive adsorption towards H^*, which hinders it is desorption and postpones H_2 generation [31–35]. For 2H-MoS_2, an n-type semiconductor, to turn the situation around, building a p-n heterojunction with another p-type semiconductor, such as MoO_3, is a feasible approach [36]. As photocatalysts, after the construction of p-n heterojunction, an inner electric field forms with the direction from n-type MoS_2 to p-type MoO_3 [37]. This produces positive charged MoS_2 and negative charged MoO_3 in p-n heterojunction [38]. The electrostatic repulsion between positive charged MoS_2 and H^* facilitates its desorption and favors H_2 production.

To synthesis MoS_2 electrocatalyst, polyoxometalates (POMs) are ideal precursors, which have achieved great successes due to unique structural features. Here, MoO_3/MoS_2, was synthesized through partial vulcanization of $[(H_2DPA)(HDPA)(PMo_{12}O_{40})]_n$ (DPA·PMo_{12}, DPA = dipyridylamine), a POM compound. Because of the existence of p-n heterojunction, MoO_3/MoS_2 exhibits superior HER activity over pure MoS_2 in both acidic and basic electrolyte. With MoO_3/MoS_2 as cathode material, an asymmetry Zn-H^+ bat-

* Corresponding author.
E-mail address: xuxx@mail.neu.edu.cn (X. Xu).

https://doi.org/10.1016/j.cclet.2022.03.071
1001-8417/

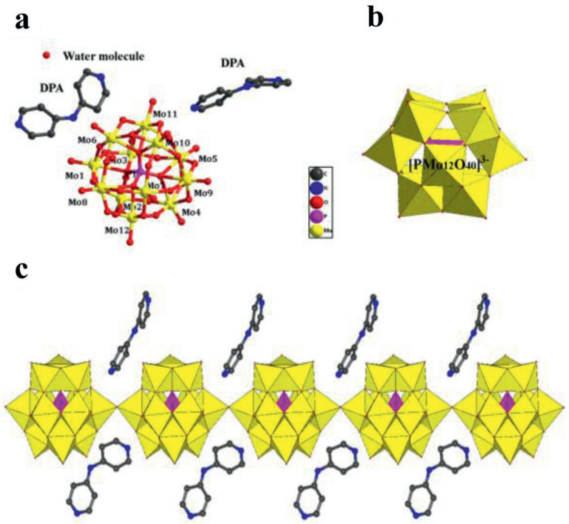

Fig. 1. (a) Fundamental unit of DPA·PMo_{12}. (b) Structure of $[PMo_{12}O_{40}]^{3-}$ cluster. (c) Structure of one-dimensional chain-like structure of DPA·PMo_{12}.

tery was built up, which achieves electric energy generation and H_2 production simultaneously. Its open circuit voltage achieves 1.11 V with short circuit current 151.4 mA/cm^2. The specific capacity and energy density of this battery reach 728 mAh/g and 759 Wh/kg at 10 mA/cm^2. Under this condition, its H_2 production rate achieves 364 μmol/h with Faradic efficiency 97.8%.

The structure of DPA·PMo_{12} was characterized by single X-ray analysis. In the fundamental unit, there exists one $[PMo_{12}O_{40}]^{3-}$ cluster and two protonated DPA molecules (Fig. 1a). In $[PMo_{12}O_{40}]^{3-}$ cluster, Mo(1) adopts distorted octahedron coordination mode with Mo(1)-O(1) = 2.303, Mo(1)-O(8) = 1.939, Mo(1)-O(13) = 1.913, Mo(1)-O(24) = 1.867, Mo(1)-O(25) = 2.048 and Mo(1)-O(31) = 1.996 Å. Mo(2) and Mo(8) exist near Mo(1), but with different bond lengths and angles. Such three MoO_6 octahedron links together with edge sharing mode and generates a Mo_3 unit (Fig. 1b). $[PMo_{12}O_{40}]^{3-}$ cluster is composed by four Mo_3 units with vertex sharing mode. Adjacent $[PMo_{12}O_{40}]^{3-}$ clusters are further connected by O(24) and generates one-dimensional chain-like structure with Mo(1)-O(24) = 1.867 Å and Mo(2)-O(24) = 1.863 Å (Fig. 1c). Protonated DPA molecules locate near this $[PMo_{12}O_{40}]^{3-}$ chain. Intensive electrostatic attraction exists between DPA and $[PMo_{12}O_{40}]^{3-}$. The structure of DPA·PMo_{12} was studied with FTIR (Fig. S1 in Supporting information). The stretching at 804 and 864 cm^{-1} originates from Mo-O-Mo. Mo=O appears at 945 cm^{-1}. The stretching located at 1051 cm^{-1} is ascribed to P-O.

The structure of vulcanized product was studied with powder X-ray diffraction (PXRD) at first. Three typical diffraction peaks belonging to 2H MoS_2 appear at 12.7°, 33.4° and 39.8°, which match with its (002), (100) and (103) planes (Fig. S2a in Supporting information) [39]. Compared with pure MoS_2, the (002) diffraction peak shifts towards low angle direction slightly and this implies the spacing between MoS_2 layers broadens, which can be ascribed to DPA insertion. Another peak located at 26.6° agrees with (040) plane of MoO_3 (35–0609). Further structural information is revealed by Raman spectrum. Two distinctive Raman peaks appear at 379.6 and 400.2 cm^{-1} originates from $E^1{}_{2g}$ and $A^1{}_g$ of 2H MoS_2, which correspond with in-plane and out-of-plane vibration modes (Fig. S2b in Supporting information). Compared with MoS_2, $E^1{}_{2g}$ and $A^1{}_g$ both move towards low wave-number direction. The interval between $E^1{}_{2g}$ and $A^1{}_g$ peaks is 20.6 cm^{-1}, which is lower than pure MoS_2. This suggests MoS_2 exists with few layer and low dimension character [40]. Some additional peaks were also

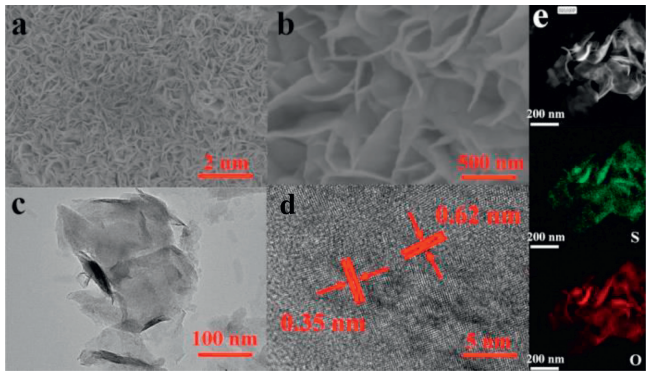

Fig. 2. (a, b) SEM images of MoO_3/MoS_2. (c) TEM image of MoO_3/MoS_2. (d) High resolution TEM image of MoO_3/MoS_2. (e) Annular dark-field TEM image and S, O elemental mapping of MoO_3/MoS_2.

detected in Raman spectrum, which located at 658.3, 812.8 and 1002.2 cm^{-1}. Their appearance confirms the existence of MoO_3 in vulcanized products [41,42].

More structural information of MoO_3/MoS_2 was revealed by X-ray photoelectron spectroscopy (XPS). In survey spectrum, the distinctive peaks can be attributed to S 2p, Mo 3d, Mo 3p and O 1s (Fig. S3 in Supporting information). Based on the content of O and S, the ratio between MoO_3 and MoS_2 is 4.2:1. In high resolution Mo 3d spectrum, three kinds of peaks appear after simulation (Fig. S4a in Supporting information). A pair of intensive doublet peak located at 230.1 and 233.2 eV matches with Mo $3d_{5/2}$ and Mo $3d_{3/2}$ of 2H-MoS_2. The remained twin peaks emerged at 233.1 and 236.7 eV can be attributed to Mo $3d_{5/2}$ and Mo $3d_{3/2}$ of Mo^{6+} in MoO_3. This further confirms co-existence of MoO_3 and MoS_2. Besides above peaks, a low single peak emerged at 226.2 eV originates from S 1s in MoS_2. In high resolution S 2p spectrum, two peaks appeared at 162.8 and 164.4 eV correspond to S $2p_{3/2}$ and S $2p_{1/2}$ of MoS_2 in 2H phase (Fig. S4b in Supporting information) [43]. In MoO_3/MoS_2, Mo $3d_{3/2}$ and Mo $3d_{5/2}$ of MoS_2 move to negative side compared with pure MoS_2 (Fig. S5). This affirms intensive interaction exists between MoO_3 and MoS_2.

The morphology of MoO_3/MoS_2 was surveyed with scanning electron microscopy (SEM), which shows flower like appearance (Fig. 2a). These flowers are constructed by two dimensional nanosheet as leaf. The size of flower leaf ranges from 200 nm to 300 nm with thickness 20–30 nm (Fig. 2b). Transmission electron microscopy (TEM) reveals more morphology information of MoO_3/MoS_2. TEM image also confirms the flower appearance of MoO_3/MoS_2, which is in accordance with SEM result (Fig. 2c). High resolution TEM (HRTEM) reveals few layer character of MoS_2 with thickness less than 10 nm. The lattice spacing about 0.62 nm is found in MoS_2, which matches with its (002) plane perfectly (Fig. 2d) [44]. In addition, new lattice spacing about 0.35 nm is detected in HRTEM image, which can be ascribed to (040) plane of MoO_3 [45]. High angle annular dark field (HAADF) image and elemental mapping suggest S and O distribute uniformly (Fig. 2e). This further confirms co-existence of MoO_3 and MoS_2 on the sample.

The band structure of MoO_3/MoS_2 was studied with UPS and UV–vis spectra. At first, their valence band energies (E_{VB}) were calculated based on UPS spectra (Figs. 3a and b). For MoS_2 and MoO_3, their secondary electron cutoff energies (abbreviated as E_{cutoff}) are 17.01 and 16.14 eV. Based on the equation $\Phi = h\nu$ - (E_{cutoff} - $E°_F$), corresponding work functions (Φ) are 4.21 and 5.08 eV, respectively. In this equation, $h\nu$ represents the energy of excited photo (21.22 eV) and $E°_F$ means Fermi level of the spectrometer after calibration [46]. UPS spectra can also reflect the difference between E_{VB} and Fermi level (E_F). For MoS_2 and MoO_3, the difference val-

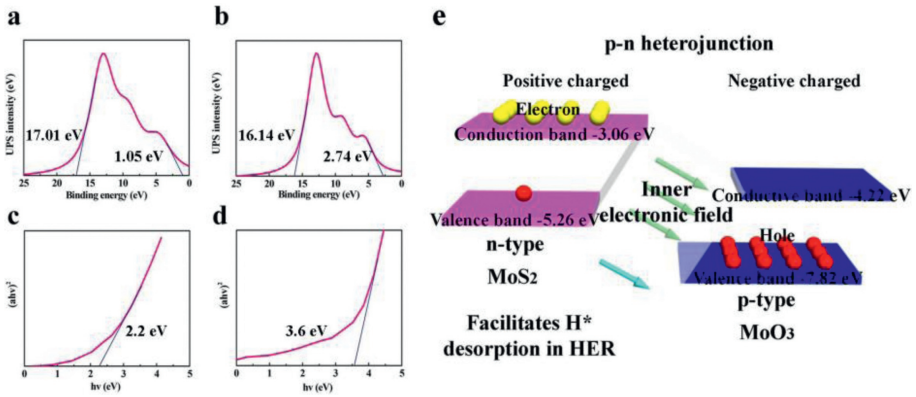

Fig. 3. Binding energy cutoff region of UPS spectra for (a) MoS_2, (b) MoO_3. Tauc plots of (c) MoS_2, (d) MoO_3. (e) Schematic diagram of p-n heterojunction.

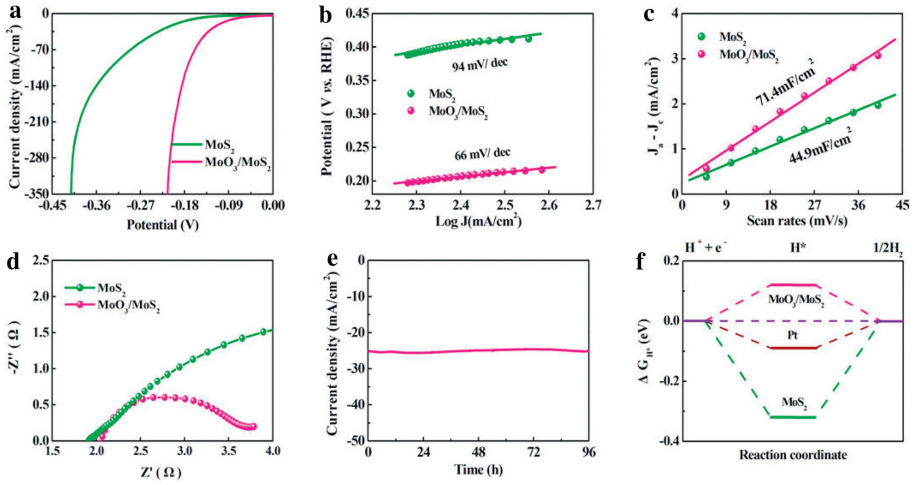

Fig. 4. (a) LSV curves; (b) Tafel slopes of MoO_3/MoS_2 and MoS_2 in 1 mol/L KOH. (c) Capacitive current as function of scan rates for MoO_3/MoS_2 and MoS_2 in 1 mol/L KOH. (d) EIS of MoO_3/MoS_2 and MoS_2. (e) Chronoampero-metric test of MoO_3/MoS_2 in 1 mol/L KOH. (f) Calculated ΔG_{H^*} for MoO_3/MoS_2, MoS_2 and Pt.

ues are 1.05 and 2.74 eV. So, E_{VB} values are −5.26 and −7.82 eV for MoS_2 and MoO_3, respectively. Their band gaps (E_g) can be calculated based on Tauc plots. For MoS_2 and MoO_3, E_g values are 2.2 and 3.6 eV (Figs. 3c and d). So, the conduction bond energy (C_B) was calculated, which are −3.06 and −4.22 eV for MoS_2 and MoO_3 [47]. The position of valence and conduction bands confirms p-n heterojunction has generated. In p-n heterojunction, an inner electric field forms with the direction from n-type MoS_2 to p-type MoO_3. This produces positive charged MoS_2 and negative charged MoO_3 in p-n heterojunction (Fig. 3e). The electrostatic repulsion between positive charged MoS_2 and H* facilitates its desorption and favors H_2 production.

HER activity of MoO_3/MoS_2 was studied by three-electrode equipment in 1 mol/L KOH. During experiment, linear sweep voltammetry (LSV) curve was measured at 5 mV/s. For MoO_3/MoS_2, the η_{10}, η_{100} and η_{200} (overpotentials to achieve 10, 100 and 200 mA/cm^2) values are 68, 173 and 198 mV (Fig. 4a). As for pure MoS_2, η_{10} is 151 mV. Moreover, it demands 325 and 393 mV to obtain 100 and 200 mA/cm^2, which are higher obviously than MoO_3/MoS_2. Tafel plot can also reveal the HER activity. For MoO_3/MoS_2, Tafel slope is 66 mV/dec (Fig. 4b). The value is lower than pure MoS_2 (94 mV/dec). This implies to drive similar current MoO_3/MoS_2 needs much lower voltage than pure MoS_2. Under acidic condition, the excellent HER activity of MoO_3/MoS_2 is still retained. In 0.5 mol/L H_2SO_4, η_{10} is 193 mV (Fig. S6 in Supporting information). This is lower than pure MoS_2 (244 mV). For MoO_3/MoS_2, η_{100} and η_{200} are 287 and 334 mV, which are also lower pure MoS_2. The merit of MoO_3/MoS_2 is also indicated by low Tafel slope of 89 mV/dec (Fig. S7 in Supporting information). In contrast, Tafel slope of MoS_2 is 105 mV/dec. The performance of MoO_3/MoS_2 is comparable with Pt/C and other HER electrocatalysts (Fig. S8 and Table S1 in Supporting information). In neutral electrolyte (1 mol/L Na_2SO_4), HER activity of MoO_3/MoS_2 becomes poor.

For MoO_3/MoS_2, to explore the root of outstanding HER activity over pure MoS_2, electrochemical active surface area (ECSA) is a landmark parameter. ECSA value is in directly proportional to electrochemical double-layer capacitance (C_{dl}) and can be simulated based on cyclic voltammetry (CV) curves under different scanning rates. CV tests of MoO_3/MoS_2 and pure MoS_2 were measured from 5 mV/s to 40 mV/s (Fig. S9 in Supporting information). The C_{dl} value of MoO_3/MoS_2 receives up to 71.4 mF/cm^2 (Fig. 4c). As for pure MoS_2, C_{dl} is only 44.9 mF/cm^2. This reveals MoO_3/MoS_2 can provide more active sites in HER. Electrochemical impedance spectroscopy (EIS) illustrates charge transfer resistance of MoO_3/MoS_2 is lower than pure MoS_2 in HER process (Fig. 4d). This ensures timely electron transportation property. Stability was investigated by chronoamperometry test at 120 mV in 1.0 mol/L KOH. After 96 h experiment, barely current decay is detected in MoO_3/MoS_2 (Fig. 4e). Stability of MoO_3/MoS_2 is revealed by successive HER test. After 8000 cycles scanning from 0 to −0.2 V, η_{100} only shifts from 173 mV to 178 mV (Fig. S10 in Supporting information). The unique HER stability of MoO_3/MoS_2 is also kept under acidic condition. LSV curves almost coincide before and after 8000 cycles HER experiment (Fig. S11 in Supporting information). Outstanding HER stability is benefit for its real application in H_2 production.

In MoO_3/MoS_2, to discover the internal relationship between MoS_2 and DPA as well as get to the deep insight into structure and HER activity, ΔG_{H^*} was calculated. It is well known that ΔG_{H^*} has been considered as a desired parameter to descript HER activity of electrocatalysts. In general, an ideal HER electrocatalyst has a ΔG_{H^*} value near 0 eV [48]. Too negative ΔG_{H^*} means excessive adsorption between electrocatalyst and H*. On the contrary, if ΔG_{H^*} is higher than 0 eV, the interaction is too weak for HER. The ΔG_{H^*} value of pure MoS_2 is −0.32 eV (Fig. 4f). This means the adsorption of MoS_2 towards H* is too intensive, which impedes its leaving and abates HER activity [49]. So, it is significant to weaken the adsorption of MoS_2 towards H*. In MoO_3/MoS_2, the ΔG_{H^*} value becomes 0.12 eV and can almost be comparable with Pt (−0.09 eV). This implies the generation of p-n heterojunction with MoO_3 can relax the adsorption towards H* and enhances HER activity.

The excellent HER activity and stability of MoO_3/MoS_2 makes it become an ideal cathode material for asymmetry Zn-H^+ battery. This asymmetry Zn-H^+ battery is built by anode chamber and cathode chamber. In anode chamber, 4.0 mol/L KOH serves as electrolyte and Zn slice is used as anode. In cathode chamber, 1.0 mol/L H_2SO_4 acts as electrolyte and MoO_3/MoS_2 is employed as cathode. Two chambers are separated by bipolar membrane, which supplies anion/cation and keep persistent current during discharge process (Fig. S12 in Supporting information). *I-V* curve of Zn-H^+ battery illustrates with the increasing of current, voltage decays gradually (Fig. S13a in Supporting information). Open circuit voltage and short circuit current of Zn-H^+ battery reach 1.11 V and 151.4 mA/cm^2. When discharge at 20 mA/cm^2, the voltage of Zn-H^+ battery achieves 0.91 V. If discharge current increases to 60 mA/cm^2, its voltage still retains at 0.69 V. Peak power density of this Zn-H^+ battery reaches 47.6 mW/cm^2 (Fig. S13b in Supporting information). This is comparable with Zn-air batteries (Table S2 in Supporting information). Discharge performance of Zn-H^+ battery was studied at 10 mA/cm^2. Based on the mass of Zn consumed during discharge, specific capacity of Zn-H^+ battery reaches 728 mAh/g (Fig. S13c in Supporting information). In this process, the energy density is 759 Wh/kg. H_2 generation ability was also assessed at 10 mA/cm^2 for 2 h (Fig. S13d in Supporting information). During this process, about 728 μmol H_2 is produced, which is close to the value in theory with Faradic efficiency 97.8%. More importantly, with this current density, Zn-H^+ battery can also provide voltage of 0.97 V. This further confirms Zn-H^+ battery can achieve electric energy generation and H_2 production simultaneously. But as a primary battery, Zn-H^+ battery cannot be recharged.

In summary, p-n heterojunction was constructed successfully in MoO_3/MoS_2 with POM compound as precursor. The inner electric field in p-n heterojunction facilitates H* desorption and improves HER activity. MoO_3/MoS_2 exhibits outstanding HER activity in both acidic and basic electrolyte with low overpotential and Tafel slope. A Zn-H^+ battery is assembled with MoO_3/MoS_2 as cathode material, which achieves electricity generation and H_2 production simultaneously. When discharge at 10 mA/cm^2, its specific capacity, energy density and H_2 production rate reach 728 mAh/g, 759 Wh/kg and 364 μmol/h Faradic efficiency achieves 97.8% in this process. We anticipate p-n heterojunction based material will play an important role in future H_2 production and electric energy generation.

Declaration of competing interest

The authors declare that they have no known competing financial interests or personal relationships that could have appeared to influence the work reported in this paper.

Acknowledgments

This work was supported by National Natural Science Foundation of China (No. 22171039); Fundamental Research Funds for the Central University (No. N2025035).

Supplementary materials

Supplementary material associated with this article can be found, in the online version, at doi:10.1016/j.cclet.2022.03.071.

References

[1] X. Li, B. Lv, X.P. Zhang, X. Jin, K. Guo, et al., Angew. Chem. Int. Ed. 61 (2021) e202114310.
[2] J.Y. Zhang, Y. Yan, B. Mei, et al., Energy Environ. Sci. 14 (2021) 365–373.
[3] Y. Yu, K. Jiang, M. Luo, et al., ACS Nano 15 (2021) 5333–5340.
[4] H. Wang, S. Zhu, J. Deng, W. Zhang, et al., Chin. Chem. Lett. 32 (2021) 291–298.
[5] C. Wei, Z.J. Xu, Chin. J. Catal. 43 (2022) 148–157.
[6] M.T. Chen, R.L. Zhang, J.J. Feng, et al., J. Colloid Interface Sci. 606 (2022) 1707–1714.
[7] Y. Cao, T. Wang, X. Li, et al., Inorg. Chem. Front. 8 (2021) 3049–3054.
[8] J. Ding, F. Wang, F. Pan, et al., ACS Catal. 11 (2021) 13721–13732.
[9] L. Zhong, H. Zhou, R. Li, et al., J. Colloid Interface Sci. 584 (2021) 439–448.
[10] M.A. Ahsan, A.R.P. Santiago, M.F. Sanad, et al., J. Colloid Interface Sci. 581 (2021) 905–918.
[11] W. Yang, W. Zhang, R. Liu, et al., Chin. J. Catal. 43 (2022) 110–115.
[12] H. Huang, H. Jung, S. Li, S. Kim, J.W. Han, J. Lee, Nano Energy 92 (2022) 106763.
[13] J. Wang, T. Liao, Z. Wei, et al., Small Methods 5 (2021) e2000988.
[14] C.G. Margarit, N.G. Asimow, A.E. Thorarinsdottir, C. Costentin, D.G. Nocera, ACS Catal. 11 (2021) 4561–4567.
[15] A. Bar-Hen, R. Bar Ziv, T. Ohaion Raz, et al., Chem. Eng. J. 420 (2021) 129771.
[16] M. Wang, L. Zhang, Y. He, H. Zhu, J. Mater. Chem. A 9 (2021) 5320–5363.
[17] P. Li, W. Li, S. Zhao, et al., Chem. Eng. J. 429 (2022) 132557.
[18] M.T. Chen, J.J. Duan, J.J. Feng, et al., Iron, J. Colloid Interface Sci. 605 (2022) 888–896.
[19] Z. Zhang, X. Wu, Z. Kou, et al., Chem. Eng. J. 428 (2022) 131133.
[20] K. Kannimuthu, K. Sangeetha, S.Sam Sankar, et al., Inorg. Chem. Front. 8 (2021) 234–272.
[21] Y. Liu, Q. Feng, W. Liu, et al., Nano Energy 81 (2021) 105641.
[22] Y. Cao, ACS Nano 15 (2021) 11014–11039.
[23] D. Kong, Y. Wang, S. Huang, et al., J. Colloid Interface Sci. 607 (2022) 1876–1887.
[24] S. Wang, L. Zhao, J. Li, X. Tian, X. Wu, L. Feng, J. Energ. Chem. 66 (2022) 483–492.
[25] D. Huang, L. Lei, R. Deng, et al., J. Catal. 381 (2020) 175–185.
[26] B.L. Li, C.B. Gong, W. Shen, et al., J. Mater. Chem. A 9 (2021) 11056–11063.
[27] X. Hou, H. Zhou, M. Zhao, Y. Cai, Q. Wei, ACS Sustainable Chem. Eng. 8 (2020) 5724–5733.
[28] W. Chen, J. Gu, Y. Du, et al., Adv. Funct. Mater. 30 (2020) 2000551.
[29] W. Zhou, M. Chen, M. Guo, et al., Nano Lett. 20 (2020) 2923–2930.
[30] M. Guan, C. Wang, S. Li, H. Du, Y. Yuan, ACS Sustainable Chem. Eng. 8 (2020) 10313–10320.
[31] D. Xie, G. Yang, D. Yu, et al., ACS Sustainable Chem. Eng. 8 (2020) 14179–14189.
[32] Y. Li, Y. Zhang, X. Tong, et al., J. Mater. Chem. A 9 (2021) 1418–1428.
[33] P.M. Pataniya, C.K. Sumesh, ACS Appl. Energy Mater. 4 (2021) 4815–4822.
[34] W. Jia, X. Wang, Z. Lu, et al., J. Alloys Compd. 885 (2021) 160990.
[35] Y. Guo, J. Tang, J. Henzie, et al., ACS Nano 14 (2020) 4141–4152.
[36] L. Deng, K. Zhang, D. Shi, et al., Appl. Catal. B 299 (2021) 120660.
[37] H. Wang, H. Zhou, L. Hu, Y. Zhang, J. Alloys Compd. 891 (2022) 161875.
[38] K. He, T. Tadesse Tsega, X. Liu, et al., Angew. Chem. Int. Ed. 58 (2019) 11903–11909.
[39] H. Liu, J.G. Wang, W. Hua, et al., Energy Stor. Mater. 35 (2021) 731–738.
[40] H. Liang, Z. Cao, F. Ming, et al., Nano Lett. 19 (2019) 3199–3206.
[41] J. Chen, Y. Liao, X. Wan, et al., J. Solid. State. Chem. 291 (2020) 121652.
[42] S. Li, Y. Liu, X. Zhao, et al., Adv. Mater. 33 (2021) e2007480.
[43] J. Liu, P. Xu, J. Liang, et al., Chem. Eng. J. 389 (2020) 124405.
[44] S. Li, Y. Liu, X. Zhao, et al., Angew. Chem. Int. Ed. 60 (2021) 20286–20293.
[45] P. Cai, J. Chen, Y. Ding, Y. Liu, Z. Wen, ACS Sustainable Chem. Eng. 9 (2021) 11524–11533.
[46] Y. Zeng, Z. Cao, J. Liao, et al., Appl. Catal. B 292 (2021) 120160.
[47] K. Chen, X.M. Zhang, X.F. Yang, et al., Appl. Catal. B 238 (2018) 263–273.
[48] Y. Zheng, X. Xu, ACS Appl. Mater. Interfaces (2020) 53739–53748.
[49] Z. Chen, Y. Song, J. Cai, et al., Angew. Chem. Int. Ed. 57 (2018) 5076–5080.